optica

# Exploiting k-space/frequency duality toward real-time terahertz imaging: supplementary material

HICHEM GUERBOUKHA, KATHIRVEL NALLAPPAN, AND MAKSIM SKOROBOGATIY*

*Engineering Physics, Polytechnique de Montréal, C. P. 6079, succ. Centre-ville, Montréal (QC) H3C 3A7, Canada*

**Corresponding author: maksim.skorobogatiy@polymtl.ca*

Published 26 January 2018

**This document provides supplementary information to "Exploiting k-space/frequency duality toward real-time terahertz imaging," https://doi.org/10.1364/OPTICA.5.000109. In this document, we first present the experimental setup used to obtain the experimental results in the main paper. Second, we develop the mathematical theory behind the spectral resolution for the cases of the binary mask and the phase mask. Finally, we study the resolution of the image reconstruction method in the two above-mentioned cases.**

## 1. Experimental setup

The experimental setup is based on a THz-time domain spectroscopy system and depicted in Fig. S1a. A Ti:Sapphire laser (100 fs, 800 nm, 100 MHz) delivers 300 mW and 10 mW to the THz photoconductive emitter and detector antennae (PCA) respectively. On the emitter side, a linear delay line is placed prior to a high-power interdigitated antenna supplied with 15 V at 5 kHz. In our setup, we use a fiber coupled detector in order to allow convenient scanning of the Fourier plane. In particular, the optical beam is focused into a polarization maintaining optical fiber with the input end rigidly fixed in the fiber coupler on the optical table, while the output end is fixed in a fiber coupler mounted on a 3D micropositioning stage. At the output end of the fiber, the beam is collimated in air before exciting the detection antenna. The optical fiber adds positive group-velocity dispersion (GVD) to the pulse, leading in a non-negligible pulse broadening that reduces the THz bandwidth of the detector. Therefore, before focusing into the fiber, the optical pulse passes through a dispersion pre-compensation system made of two diffraction gratings and a mirror that adds negative GVD to the pulse. The output current of the antenna is amplified with a lock-in amplifier before being recorded by a data acquisition card connected to a computer. Thus, the acquired data is a current proportional to the electric field as a function of time. A temporal Fourier transform is then performed on the pulse to get the amplitude and phase as a function of the THz frequency. Finally, the hybrid inverse transform described in the paper is applied in order to retrieve the field distribution in the object plane.

The optical fiber adds positive group-velocity dispersion (GVD) to the pulse, leading to a non-negligible pulse broadening that reduces the THz bandwidth of the detector. Therefore, before focusing into the fiber, the optical pulse is passed through a dispersion pre-compensation system made of two diffraction gratings and a mirror (Fig. S1b). To counterbalance the fiber's positive GVD, this system adds negative GVD as detailed in [1]:

$$GVD[\mathrm{s}^2] = -\frac{\lambda^3 d}{\pi c^2 \Lambda^2}\left[1-\left(\frac{\lambda}{\Lambda}-\sin\theta\right)^2\right]^{3/2} \qquad \textbf{(S1)}$$

where $\lambda$ is the central wavelength, $c$ is the speed of light, $\Lambda$ is the groove distance of the gratings, $d$ is the distance between the gratings and $\theta$ is

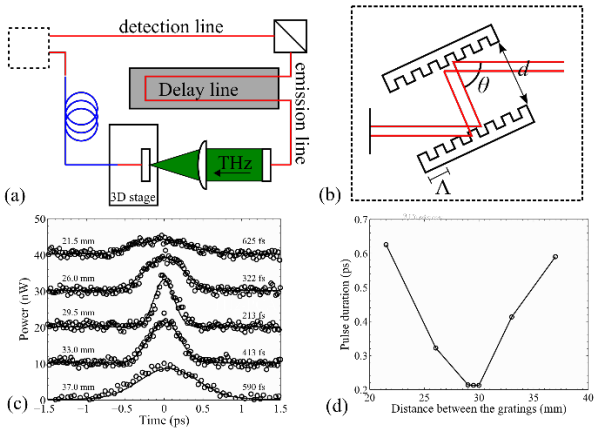


**Fig. S1.** Experimental setup. (a) Fiber-coupled THz-TDS. The red lines refer to the free-space beam, while the blue line is the optical fiber. (b) Dispersion compensation system with two diffraction gratings. (c) Autocorrelation traces for different distances between the gratings. The curves are fitted with a Gaussian function. (d) Pulse duration (full width at half maximum) as a function of the distance between the gratings.

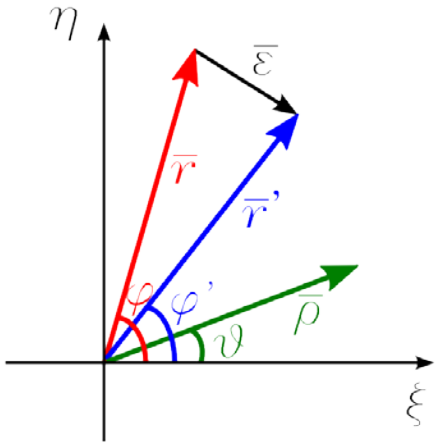


**Fig. S2.** Definition of various integration variables used throughout the paper.

the incident angle defined in Fig. S1b. By adjusting the geometrical parameters $d$ and $\theta$, it is possible to counterbalance the positive GVD of the fiber, and therefore minimize the pulse duration at the output of the fiber. In Fig. S1c, we present several autocorrelation traces of the pulse for different values of $d$, recorded using an autocorrelator kit from Newport. As it can be seen in Fig. S1d, the pulse duration is minimized to 213 fs when using $d = 29.5$ mm between the gratings. We note that the compensation system only corrects for positive GVD. In the meantime, negative GVD due to the third order dispersion or non-linear effects still occur in the fiber and are not compensated by our system. Therefore, in our system, we still have a pulse broadening. Also, in principle, one could use a dispersion compensation fiber at 1550 nm since THz emitters and detectors are commercially available at that wavelength.

## 2. Mathematical theory

### 2.1. A closer look at the image reconstruction algorithm

The objective of this section is to determine what image is retrieved when using the hybrid inverse transform presented by equation (8). As the integral (7) used in the reconstruction integrates information about the object over all frequencies, the reconstructed image $\tilde{S}(\bar{r})$ is different from the original image $S(\bar{r},\nu)$. In order to understand how $\tilde{S}(\bar{r})$ is related to the original image $S(\bar{r},\nu)$, we substitute the optical Fourier transform of the image $U(\bar{\rho},\nu)$ as measured in the Fourier plane of our setup (equation (5)) into the hybrid inverse transform developed in this paper (equation (7)) and get:

$$\tilde{S}(\bar{r}) = \iint d\theta\nu d\nu \iint d\varphi' r' dr' \left(\frac{\rho_0}{cF}\right)^2 \frac{S(\bar{r}',\nu)}{U_{\text{ref}}(\nu)} \exp\left[-\frac{j2\pi\nu}{cF}\bar{\rho}_0\cdot(\bar{r}'-\bar{r})\right] \quad \textbf{(S2)}$$

where $r'$ and $\phi'$ are the integration variables that are defined in Fig. S2. We can simplify the expressions above by defining $\bar{\varepsilon} = \bar{r}' - \bar{r}$ and $\phi_{\bar{\varepsilon}}$ as shown in Fig. S2. Then, equation (S2) can be written as:

$$\begin{aligned}\tilde{S}(\bar{r}) &= \iint d\theta\nu d\nu \iint d\varphi_{\bar{\varepsilon}}\varepsilon d\varepsilon' \left(\frac{\rho_0}{cF}\right)^2 \frac{S(\bar{r}+\varepsilon,\nu)}{U_{\text{ref}}(\nu)} \exp\left[-\frac{j2\pi\nu}{cF}\bar{\rho}_0\cdot\bar{\varepsilon}\right] \quad \textbf{(S3)}\\ &= \iint d\theta\nu d\nu \iint d\varphi_{\bar{\varepsilon}}\varepsilon d\varepsilon' \left(\frac{\rho_0}{cF}\right)^2 \frac{S(\bar{r}+\varepsilon,\nu)}{U_{\text{ref}}(\nu)} \exp\left[-\frac{j2\pi\nu}{cF}\rho_0\varepsilon\cos(\theta-\varphi_{\bar{\varepsilon}})\right]\end{aligned}$$

The integral above can be further simplified by integrating over $\theta$, thus arriving to the following final expression for the hybrid inverse transform:

$$\tilde{S}(\bar{r}) = 2\pi\int_0^\infty \nu d\nu \int_0^{2\pi} d\varphi_{\bar{\varepsilon}} \int_0^\infty \varepsilon d\varepsilon \left[\left(\frac{\rho_0}{cF}\right)^2 \frac{S(\bar{r}+\bar{\varepsilon},\nu)}{U_{\text{ref}}(\nu)}\right] J_0\left(\frac{2\pi\rho_0}{cF}\nu\varepsilon\right) \quad \textbf{(S4)}$$

where we have used the integral representation of the Bessel function from the Supplementary Section 3 (equation S2). In order to continue further, we now need to specify the structure of the original image $S(\bar{r},\nu)$. In the following sections, we consider two particular types of images – those based on amplitude or phase masks.

### 2.2. Amplitude masks

First, we consider the case of space-frequency separable amplitude masks that result in the image of the general form $S(\bar{r},\nu) = S(\bar{r})E(\nu)$. We find that when using the reference function $U_{\text{ref}}(\nu)$ as defined by equation (11), the hybrid inverse transform (expression (S4)) gives the following:

$$\tilde{S}(\bar{r}) = \frac{2\pi}{\iint d\bar{r}S(\bar{r})}\left(\frac{\rho_0}{cF}\right)^2 \int_0^{2\pi} d\varphi_{\bar{\varepsilon}} \int_0^\infty \varepsilon d\varepsilon S(\bar{r}+\bar{\varepsilon}) \int_0^\infty \nu d\nu J_0\left(\frac{2\pi\rho_0\varepsilon}{cF}\nu\right) \quad \textbf{(S5)}$$

The last integral can be readily evaluated analytically using integral representations of the delta function (equation S21) in terms of the Bessel functions:

$$\int_0^\infty \nu d\nu J_0\left(\frac{2\pi\rho_0\varepsilon}{cF}\nu\right) = \frac{cF}{2\pi\rho_0\varepsilon}\delta\left(\frac{2\pi\rho_0\varepsilon}{cF}\right) \quad \textbf{(S6)}$$

where $\delta(2\pi\rho_0\varepsilon/cF)$ is the Dirac delta function. Then,

$$\tilde{S}(\bar{r}) = \frac{1}{\iint d\bar{r}S(\bar{r})}\frac{\rho_0}{cF}\int_0^{2\pi} d\varphi_{\bar{\varepsilon}} \int_0^\infty \varepsilon d\varepsilon S(\bar{r}+\bar{\varepsilon})\delta\left(\frac{2\pi\rho_0\varepsilon}{cF}\right) \quad \textbf{(S7)}$$

These integrals can then be evaluated analytically by using the properties of the Dirac delta function (equation S22):

$$\tilde{S}(\bar{r}) = \frac{S(\bar{r})}{\iint d\bar{r}S(\bar{r})} \quad \textbf{(S8)}$$

where the denominator is simply a constant proportional to the area of the image. Therefore, we conclude that in the case of a space-frequency separable amplitude mask, the hybrid inverse transform of the Fourier image results in the original image normalized by the area of the image. If the maximum frequency used in the reconstruction is finite, we can also use equation (S5) in order to estimate the resultant image resolution as demonstrated in the Section 3.1 below.

### 2.2. Phase masks

We now consider the case of phase masks that result in the image of the general form $S(\bar{r},\nu) = S(\bar{r})E(\nu)\exp\left[j2\pi\nu\left(\Delta_0 - \mu(\bar{r})\right)/c\right]$. As for the choice of the reference function $U_{\text{ref}}(\nu)$ in the inversion algorithm (S4), one would be tempted to use the same normalization as in the case of amplitude masks. However, as we will see in what follows, in order to ensure convergence of all the integrals, we need to modify the reference function. Particularly, in the case of phase masks we define the reference $U_{\text{ref}}(\nu)$ as the Fourier transform of a pulse at the origin of the k-space ($\rho_0 = 0$), measured using a flat reference sample $\mu(\bar{r}) = 0$:

$$U_{\text{ref}}(\nu) = \nu^m \frac{jcF}{\nu}U(0,\nu) = \nu^m E(\nu)\exp\left(\frac{j2\pi\nu\Delta_0}{c}\right)\iint d\bar{r}S(\bar{r}) \quad \textbf{(S9)}$$

where $\nu^m$ is an additional frequency multiplier with an exponent $m$ that must be chosen to ensure the convergence of the inversion algorithm. Using expression (S4) for the hybrid inverse transform together with the reference function defined in (S9), we find:

$$\tilde{S}(\vec{r}) = \frac{2\pi}{\iint d\vec{r} S(\vec{r})}\left(\frac{\rho_0}{cF}\right)^2 \int_0^{2\pi} d\varphi_{\vec{\varepsilon}} \int_0^{\infty} \varepsilon d\varepsilon S(\vec{r}+\vec{\varepsilon}) K_m(\vec{r},\vec{\varepsilon}) \quad \textbf{(S10)}$$

where we define:

$$K_m = \int_0^{\infty} \nu^{1-m} d\nu \exp\left[-\frac{j2\pi\nu}{c}\mu(\vec{r}+\vec{\varepsilon})\right] J_0\left(\frac{2\pi\rho_0\varepsilon}{cF}\nu\right) \quad \textbf{(S11)}$$

In the case of amplitude masks considered earlier, we used $m = 0$, however, in the case of phase masks this choice generally results in the divergence of the integral (S10). Indeed, using basic properties of the Bessel function (equation S26) we find that:

$$K_0(\vec{r},\vec{\varepsilon}) = \left(\frac{c}{2\pi}\right)^2\left(\frac{F}{\rho_0}\right)^2 \mu_0(\vec{r}) \cdot \begin{cases} \frac{-1}{\left[\mu_0(\vec{r}+\vec{\varepsilon})^2 - \varepsilon^2\right]^{3/2}} & \text{if } 0 < \varepsilon < \mu_0(\vec{r}+\vec{\varepsilon}) \\ \frac{j}{\left[\varepsilon^2 - \mu_0(\vec{r}+\vec{\varepsilon})^2\right]^{3/2}} & \text{if } \varepsilon > \mu_0(\vec{r}+\vec{\varepsilon}) \end{cases} \quad \textbf{(S12)}$$

where the normalized optical path is defined as $\mu_0(\vec{r}+\vec{\varepsilon}) = F/\rho_0\,\mu(\vec{r}+\vec{\varepsilon})$. Therefore, the integration over $\varepsilon$ in equation (S10) can be divided into the sum of two integrals over different regions of $\varepsilon$ values. From the form of (S12) it follows that generally both of these integrals are divergent, thus rendering $\tilde{S}(\vec{r})$ ill defined. Therefore, $m = 0$ is not an acceptable choice for the reference function.

On the other hand, if we select $m = 1$, then, using equation (S27),

$$K_1(\vec{r},\vec{\varepsilon}) = \frac{cF}{2\pi\rho_0} \cdot \begin{cases} \frac{-j}{\sqrt{\mu_0(\vec{r}+\vec{\varepsilon})^2 - \varepsilon^2}} & \text{if } 0 < \varepsilon < \mu_0(\vec{r}+\vec{\varepsilon}) \\ \frac{1}{\sqrt{\varepsilon^2 - \mu_0(\vec{r}+\vec{\varepsilon})^2}} & \text{if } \varepsilon > \mu_0(\vec{r}+\vec{\varepsilon}) \end{cases} \quad \textbf{(S13)}$$

where again $\mu_0(\vec{r}+\vec{\varepsilon}) = F/\rho_0\,\mu(\vec{r}+\vec{\varepsilon})$. Now, we can write equation (S10) as the sum of the two integrals:

$$\tilde{S}(\vec{r}) = \frac{2\pi}{\iint d\vec{r} S(\vec{r})}\left(\frac{\rho_0}{cF}\right)^2 \int_0^{2\pi} d\varphi_{\vec{\varepsilon}} \left[S_{\varepsilon<\mu_0(\vec{r}+\vec{\varepsilon})} + S_{\varepsilon>\mu_0(\vec{r}+\vec{\varepsilon})}\right] \quad \textbf{(S14)}$$

where

$$S_{\varepsilon<\mu_0(\vec{r}+\vec{\varepsilon})} = -\frac{jcF}{2\pi\rho_0}\int_0^{\mu_0(\vec{r}+\vec{\varepsilon})} d\varepsilon \frac{\varepsilon \cdot S(\vec{r}+\vec{\varepsilon})}{\sqrt{\mu_0(\vec{r}+\vec{\varepsilon})^2 - \varepsilon^2}} \quad \textbf{(S15)}$$

and

$$S_{\varepsilon>\mu_0(\vec{r}+\vec{\varepsilon})} = \frac{cF}{2\pi\rho_0}\int_{\mu_0(\vec{r}+\vec{\varepsilon})}^{\infty} d\varepsilon \frac{\varepsilon \cdot S(\vec{r}+\vec{\varepsilon})}{\sqrt{\varepsilon^2 - \mu_0(\vec{r}+\vec{\varepsilon})^2}} \quad \textbf{(S16)}$$

We note that the contribution $S_{\varepsilon>\mu_0(\vec{r}+\vec{\varepsilon})}$ is purely real, and it is generally divergent if the function $S(\vec{r}+\vec{\varepsilon})$ (amplitude mask) is not zero at infinity. In the meantime, the contribution $S_{\varepsilon<\mu_0(\vec{r}+\vec{\varepsilon})}$ is purely imaginary and is always finite. Moreover, if the spatial region of the optical path variation $\mu(\vec{r})$ is large enough so its value can be considered constant $\mu_0(\vec{r}+\vec{\varepsilon}) = \mu_0(\vec{r})$ inside a circle of radius $\varepsilon \sim \mu_0(\vec{r})$, and if a similar condition is respected by the amplitude mask $S(\vec{r})$, then we can evaluate equation (S15) exactly:

$$\begin{aligned} S_{\varepsilon<\mu_0(\vec{r}+\vec{\varepsilon})} &= -\frac{jcF}{2\pi\rho_0}\int_0^{\mu_0(\vec{r}+\vec{\varepsilon})} d\varepsilon \frac{\varepsilon \cdot S(\vec{r}+\vec{\varepsilon})}{\sqrt{\mu_0(\vec{r}+\vec{\varepsilon})^2 - \varepsilon^2}} \\ &= -\frac{jcF}{2\pi\rho_0} S(\vec{r})\int_0^{\mu_0(\vec{r}+\vec{\varepsilon})} d\varepsilon \frac{\varepsilon}{\sqrt{\mu_0(\vec{r}+\vec{\varepsilon})^2 - \varepsilon^2}} \\ &= -\frac{jcF}{2\pi\rho_0} S(\vec{r})\mu_0(\vec{r}) \end{aligned} \quad \textbf{(S17)}$$

Therefore, from equation (S14), we find that the imaginary part of the hybrid inverse transform $\tilde{S}(\vec{r})$ computed with $m = 1$ is proportional to the spatial variation of the optical path in the image plane:

$$\mathrm{Im}\{\tilde{S}(\vec{r})\} = -\frac{2\pi}{c}\frac{S(\vec{r})}{\iint d\vec{r} S(\vec{r})}\mu(\vec{r}) \quad \textbf{(S18)}$$

If the maximum frequency used in the reconstruction is finite, we can also use equation (S10) in order to estimate the resultant image resolution as demonstrated below in Supplementary section 3.2.P

### 2.3. Mathematical identities

In this section, we list various mathematical identities used throughout the paper.

*Integral representation of the Bessel function of a real argument and some of its basic properties*

$$J_0(x) = \frac{1}{2\pi}\int_0^{2\pi} d\theta \exp\left(\pm jx\cos\theta\right) \quad \textbf{(S19)}$$

$$J_1(ax) = -\frac{1}{a} J_0\,'(ax) \quad \textbf{(S20)}$$

*Direct delta function, properties and integral representations*

$$\delta(x) = \int_{-\infty}^{\infty} d\theta \exp\left(\mathrm{j}2\pi x\xi\right) \quad \textbf{(S21)}$$

$$\delta(ax) = \frac{1}{|a|}\delta(x) \quad \textbf{(S22)}$$

$$\int_0^{\infty} xJ_0(ax)dx = \frac{1}{a}\delta(a) \quad \textbf{(S23)}$$

$$\int_{-\infty}^{\infty} f(x)\delta(x)dx = f(0) \quad \textbf{(S24)}$$

*Some integrals involving the Bessel functions*

$$\int_0^{\infty} uJ_0(au)dx = \frac{x}{a}J_1(ax) \quad \textbf{(S25)}$$

$$\int_0^{\infty} x\exp\left(-jax\right)J_0(bx)dx = \begin{cases} \frac{ja}{\left(b^2-a^2\right)^{3/2}} & \text{if } |b|>|a| \\ \frac{-a}{\left(a^2-b^2\right)^{3/2}} & \text{if } |a|>|b| \end{cases} \quad \textbf{(S26)}$$

$$\int_0^{\infty} \exp\left(-jax\right)J_0(bx)dx = \begin{cases} \frac{1}{\sqrt{b^2-a^2}} & \text{if } |b|>|a| \\ \frac{-j\,\mathrm{sgn}(a)}{\sqrt{a^2-b^2}} & \text{if } |a|>|b| \end{cases} \quad \textbf{(S27)}$$

## 3. Resolution of the reconstructed images

### 3.1. Resolution of the amplitude masks

The image resolution in the case of amplitude masks can be readily deduced from the hybrid inverse transform equation (S5):

$$\tilde{S}(\vec{r}) = \frac{2\pi}{\iint d\vec{r} S(\vec{r})}\left(\frac{\rho_0}{cF}\right)^2 \int_0^{2\pi} d\varphi_{\vec{\varepsilon}} \int_0^{\infty} \varepsilon d\varepsilon S(\vec{r}+\vec{\varepsilon}) \int_0^{\infty} \nu d\nu J_0\left(\frac{2\pi\rho_0\varepsilon}{cF}\nu\right) \quad \textbf{(S28)}$$

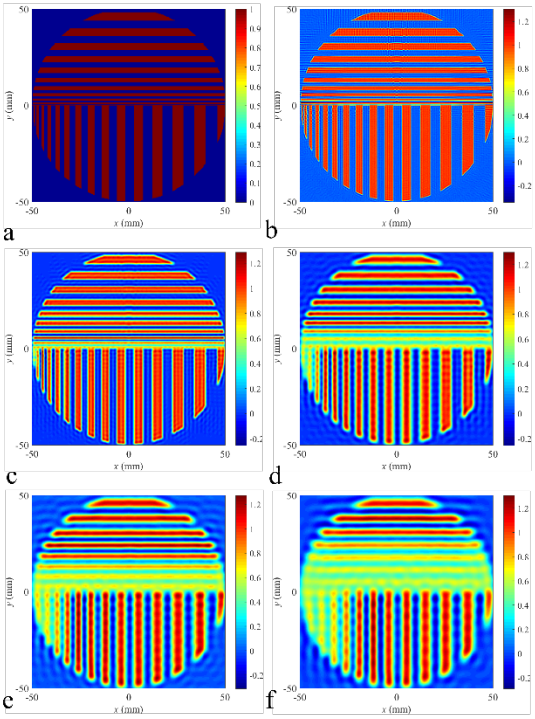


**Fig. S3.** Numerical reconstruction of a binary mask of 400 μm minimal line width. (a) Target image featuring pairs of "ones" and "zeros" lines of increasing widths. The smallest line width is 400 μm, the increment in the line width is also 400 μm. (b) Image reconstruction using hybrid inverse transform (equation (12)) with $\lambda_{min}$=150 μm ($\nu_{max}$=2 THz), (c) $\lambda_{min}$=350 μm ($\nu_{max}$=0.86 THz), (d) $\lambda_{min}$=600 μm ($\nu_{max}$=0.5 THz), (e) $\lambda_{min}$=800 μm ($\nu_{max}$=0.375 THz) and (f) $\lambda_{min}$=1000 μm ($\nu_{max}$=0.3 THz).

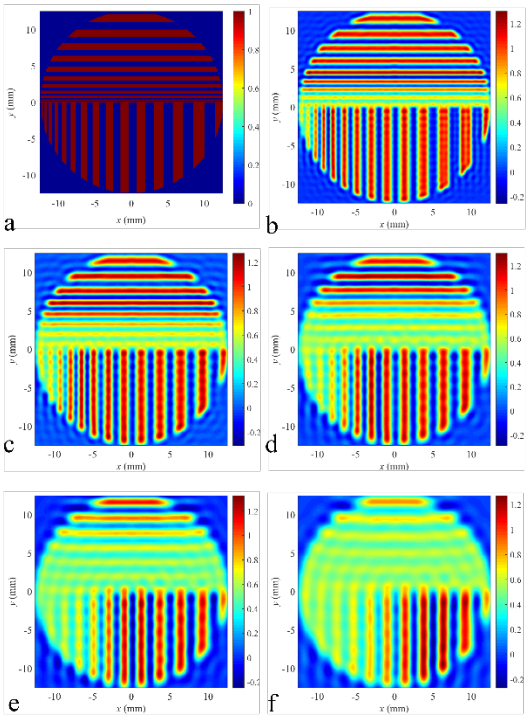


**Fig. S4.** Numerical reconstruction of a binary mask of 100 μm minimal line width. (a) Target image featuring pairs of "ones" and "zeros" lines of increasing widths. The smallest line width is 100 μm, the increment in the line width is also 100 μm. (b) Image reconstruction using hybrid inverse transform (equation (12)) with $\lambda_{min}$=150 μm ($\nu_{max}$=2 THz), (c) $\lambda_{min}$=200 μm ($\nu_{max}$=1.5 THz), (d) $\lambda_{min}$=250 μm ($\nu_{max}$=1.2 THz), (e) $\lambda_{min}$=300 μm ($\nu_{max}$=1 THz) and (f) $\lambda_{min}$=350 μm ($\nu_{max}$=0.86 THz).

We note that, as the probing pulse has a finite duration (bandwidth limited pulse), the maximal frequency in the integral presented above is limited to $\nu_{max}$. This also sets the minimal resolution achievable by the hybrid inverse transform, which, as we show below, is proportional to the smallest probed wavelength ($\lambda_{min} = c/\nu_{max}$). To demonstrate this point mathematically, we consider the last integral in equation (S28). However, instead of integrating to infinity, we now integrate up to $\nu_{max}$. In this case, using the Bessel identity (equation (S25)), the last integral of equation (S28) becomes:

$$\int_0^{\nu_{max}} \nu d\nu J_0\left(\frac{2\pi\rho_0\varepsilon}{cF}\nu\right) = \frac{cF\nu_{max}}{2\pi\rho_0\varepsilon} J_1\left(\frac{2\pi\rho_0\varepsilon}{cF}\nu_{max}\right) \quad \textbf{(S29)}$$

Then, by using the property (S24), equation (S28) transforms into:

$$\begin{aligned}\tilde{S}(\vec{r}) &= \frac{\nu_{max}}{\iint d\vec{r}S(\vec{r})}\frac{\rho_0}{cF}\int_0^{2\pi} d\varphi_{\vec{\varepsilon}}\int_0^{\infty} d\varepsilon S(\vec{r}+\vec{\varepsilon})J_1\left(\frac{2\pi\rho_0\varepsilon}{cF}\nu_{max}\right) \\ &= -\frac{1}{2\pi\iint d\vec{r}S(\vec{r})}\int_0^{2\pi} d\varphi_{\vec{\varepsilon}}\int_0^{\infty} d\varepsilon S(\vec{r}+\vec{\varepsilon})J_0'\left(\frac{2\pi\rho_0\varepsilon}{cF}\nu_{max}\right) \\ &= \frac{1}{2\pi\iint d\vec{r}S(\vec{r})}\int_0^{2\pi} d\varphi_{\vec{\varepsilon}}\left[S(\vec{r})+\int_0^{\infty} d\varepsilon\frac{\partial S(\vec{r}+\vec{\varepsilon})}{\partial\varepsilon}J_0\left(\frac{2\pi\rho_0\varepsilon}{cF}\nu_{max}\right)\right] \\ &= \frac{S(\vec{r})}{\iint d\vec{r}S(\vec{r})}+\frac{1}{2\pi\iint d\vec{r}S(\vec{r})}\int_0^{2\pi} d\varphi_{\vec{\varepsilon}}\int_0^{\infty} d\varepsilon\frac{\partial S(\vec{r}+\vec{\varepsilon})}{\partial\varepsilon}J_0\left(\frac{2\pi\rho_0\varepsilon}{cF}\nu_{max}\right)\end{aligned} \quad \textbf{(S30)}$$

From equation (S30), we note that the leading expression for the hybrid inverse transform in the case of a bandwidth limited pulse is still proportional to the value of the original image, with a correction term featuring an integration of the amplitude mask spatial derivative over a fast-varying sign-changing Bessel function of a large argument. The main contribution to this integral comes from averaging the amplitude mask derivative inside a circle of radius $\varepsilon \sim \lambda_{min} F/\rho_0$. From this, we conclude that the fundamental limit of the spatial resolution in the case of the amplitude mask is set by the finite bandwidth of the probing pulse and is $\sim\lambda_{min} F/\rho_0$, where $\lambda_{min}$ is the smallest wavelength probed by the pulse. This result correlates well with the Nyquist theorem for the Fourier transform discussed in the paper.

To confirm this result, we perform numerical simulations using, as an object, a binary mask featuring a pattern of lines of increasing size of ones (full transmittance) and zeros (full absorbance) (Fig. S3a). In Fig. S3a, the smallest line of "ones" has a width of 400 μm followed by an adjacent line of "zeros" of the same size. The pairs of lines are then repeated with increasing size in increments of 400 μm (i.e. 400 μm, 800 μm, 1200 μm etc.). We then compute the direct transform given by equation (1) for all the frequencies specified by the THz pulse bandwidth (0.1 - 2 THz with a step of 1 GHz). Then, using the hybrid inverse transform (equation (12)) we reconstruct the original image. In Fig. S3b to S3f, we present several reconstructed images for different values of the maximal THz frequency used in the hybrid inverse transform. In Fig. S4, we perform the same numerical simulations for a geometrically similar image that feature thinner lines (a minimal width of 100 μm and a step of 200 μm in the width increment between the pairs of the adjacent lines). Just by looking at the images, as expected, we find qualitatively that the resolution improves when the THz bandwidth increases.

From these numerical results, we can estimate the dependence of the spatial resolution of the images obtained using the hybrid inverse transform (12) as a function of the maximal THz frequency used in the reconstruction. To do so, for each line of "zeros" and "ones", we calculate the average reconstructed intensities $I_1$ and $I_0$ at the positions where the corresponding lines should be. We the

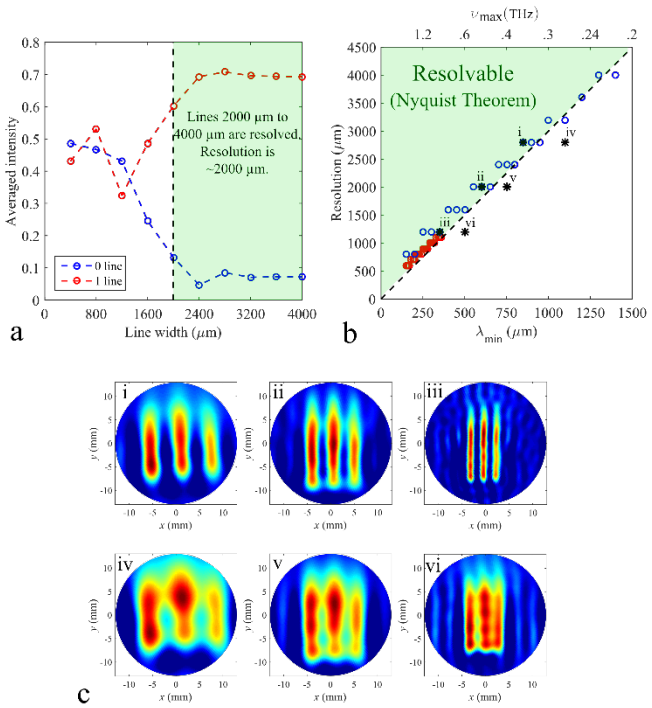


**Fig. S5.** Image resolution, case of the amplitude masks. (a) Definition of the resolution using averaged values at the location of "ones" and "zeros". (b) Resolution of amplitude masks as a function of the THz bandwidth. The green region corresponds to the resolvable region set by the Nyquist theorem. The blue and red circles correspond to Fig. S3 and S4 respectively. (c) Experimental measurements using three different amplitude masks featuring three cutout lines. Reconstructed images of the amplitude masks as a function of λ_min (ν_max). i. Lines of 2800 μm with $\lambda_{min}$=850 μm ($\nu_{max}$=0.35 THz) and iv. $\lambda_{min}$=1100 μm ($\nu_{max}$=0.27 THz); ii. lines of 2000 μm with $\lambda_{min}$=600 μm ($\nu_{max}$=0.5 THz) and v. $\lambda_{min}$=750 μm ($\nu_{max}$=0.4 THz); iii. lines of 1200 μm with $\lambda_{min}$=300 μm ($\nu_{max}$=1 THz) and vi. $\lambda_{min}$=500 μm ($\nu_{max}$=0.6 THz).

plot these averaged values for each line. If the line of "ones" is resolved, one should thus find an averaged value close to one at the line location. Similarly, if the line of "zeros" is resolved, one should find an averaged value close to zero at the corresponding line location. The adjacent "zero" and "one" lines are considered not resolved if the corresponding averaged values for these lines become comparable, that is $(I_1 - I_0)/(I_1 + I_0) < 0.5$. To illustrate this, in Fig. S5a, we present the averaged intensities at the locations of "zeros" and "ones" in the case of $\lambda_{\min} = 600$ μm ($\nu_{\max} = 0.5$ THz). The lines from 400 μm to 1600 μm are not resolvable since "zeros" and "ones" have comparable averaged values. However, starting with a 2000 μm thick line, the lines can be readily resolved according to the condition presented above. From this, we conclude that in the case of $\lambda_{\min} = 600$ μm, the minimal achievable resolution is ~2000 μm.

We then perform the same analysis for other values of $\lambda_{\min}$ (various THz pulse bandwidths) and present the results in Fig. S5b. The dotted line corresponds to the resolution set by the Nyquist theorem: $\delta x = 0.5\,\lambda_{\min} F/\rho_0$, while in circles, we present the resolutions found using the approach described above. From this, we confirm that the resolution of the binary amplitude mask indeed follows closely the prediction of the Nyquist theorem. This is further confirmed experimentally in Fig. S5c. There, we use three different binary masks in the form of metal plates with cutouts in the shape of lines. Each amplitude mask features three cutouts in the form of lines of 15 mm in length and widths of 2800 μm, 2000 μm and 1200 μm that are separated by the same width from each other. Then, using our Fourier optics setup and the hybrid inverse algorihm we reconstruct the images of the three lines using different values of the maximal frequency $\nu_{\max}$ in the integral (12) (different THz bandwidths). The inserts i, ii, iii in the top row of Fig. S5c show images of the three different amplitude masks that were reconstructed using $\lambda_{\min}$ (850 μm, 600 μm, 300 μm respectively). According to the Nyquist theorem, these wavelengths are small enough to correctly resolve the lines in the corresponding amplitude masks, which is indeed what is observed experimentally. At the same time, in the bottom row of Fig. S5c (inserts iv, v, vi), we show images of the same three amplitude masks that were reconstructed using $\lambda_{\min}$ of 1100 μm, 750 μm, and 500 μm respectively. According to the Nyquist theorem, these values of $\lambda_{\min}$ are insufficient to resolve the lines in the coresponding amplitude masks, which is indeed what is confirmed experimentally. From this we conclude that, indeed, our analysis of the image resolution in the case of amplitude masks agrees well with the classical Nyquist theorem applied to the classical Fourier optics systems.

### 3.2. Resolution of the phase masks

In the case of phase masks, we have demonstrated earlier that the imaginary part of the hybrid inverse transform is, in some limit, simply proportional to the local optical path incurred by the light due to the passage through the phase mask:

$$\begin{aligned}\mathrm{Im}\left\{\tilde{S}(\vec{r})\right\} &= -\frac{1}{\iint d\vec{r} S(\vec{r})}\frac{\rho_0}{cF}\int_0^{2\pi} d\varepsilon \frac{\varepsilon \cdot S(\vec{r}+\vec{\varepsilon})}{\sqrt{\mu_0(\vec{r}+\vec{\varepsilon})^2 - \varepsilon^2}} \\ &= -\frac{jcF}{2\pi\rho_0} S(\vec{r})\int_0^{\mu_0(\vec{r}+\vec{\varepsilon})} d\varepsilon \frac{\varepsilon}{\sqrt{\mu_0(\vec{r}+\vec{\varepsilon})^2 - \varepsilon^2}} \\ &= -\frac{2\pi}{c}\frac{S(\vec{r})\mu(\vec{r})}{\iint d\vec{r} S(\vec{r})}\end{aligned} \quad \textbf{(S31)}$$

This result is strictly valid in the case of piecewise constant phase masks if the value of the normalized optical path $\mu_0(\vec{r})$ and the value of the amplitude mask $S(\vec{r})$ are constant within the circle of radius $\varepsilon = \mu_0(\vec{r} + \vec{\varepsilon})$.This result, however, breaks in the vicinity of the boundaries between different optical path regions of the phase mask. We therefore conclude that in the case of the hybrid inverse transform applied to the phase masks, there is a fundamental limit to the resolution of such a transform which is set by the local value of the normalized optical path length $\mu_0(\vec{r}) = \mu(\vec{r})\,F/\rho_0 = h(\vec{r})(n_m - n_a)$. Therefore, in the case of phase masks, a correction term needs to be added to the resolution given by the Nyquist theorem:

$$\delta x = \left[0.5\lambda_{\min} + h(n_m - n_a)\right]\cdot\frac{F}{\rho_0} \quad \textbf{(S32)}$$

To confirm this prediction, we perform numerical simulations using as target images phase masks featuring geometrical patterns of lines identical to those of amplitude masks presented in Figs. S3 and S4. In the case of phase masks, however, we consider as lines shallow scratches of depth $h$ engraved onto a plastic plate of refractive index $n_m = 1.62$ (Fig. S6a). For the reconstruction of the engraving pattern we use the hybrid inverse transform (17) corresponding to the case of the phase masks. In Fig. S6b to S6f, we present the reconstructed optical paths for different values of the line depth $h$ and the same THz bandwidth ($\lambda_{\min}$ fixed to 150 μm). As expected from (S32), the resolution improves as the scratch depth decreases.

With a definition of the resolution similar to the binary amplitude mask ("ones" are the lines corresponding to engravings, "zeros" are the lines where there is no engraving), we numerically find the resolution for different THz bandwidths and optical thicknesses. In Fig. S7a, we plot the resolution as a function of the THz bandwidth for different values of the engraving depth. The dotted line in the figure has the equation $\delta x = 0.5\,\lambda_{\min}\,F/\rho_0$ and corresponds to the fundamental limit set by the Nyquist theorem. From the figure, we confirm that the minimal resolution is indeed set by the Nyquist theorem. At the same time, the resolution can be considerably worse than that predicted by the Nyquist theorem due to the contribution proportional to the optical path length of the engraving, which can be significant for deep engravings. Thus, in Fig. S7b, we plot this limit as a function of the engraving depths. There, the dotted line follows the equation $\delta x = h(n_m - n_a)\,F/\rho_0$ and it defines the fundamental limit to the resolution in case of the phase masks in the limit of an infinite pulse bandwidth.

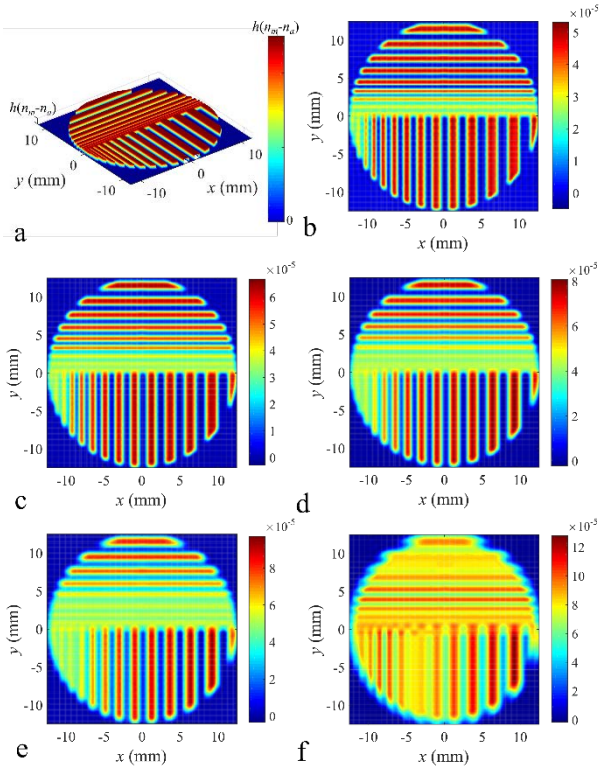


**Fig. S6.** Numerical reconstruction of a phase mask of 100 μm minimal line width. (a) Target image featuring pairs of "ones" and "zeros" lines of increasing widths. The smallest line width is 100 μm, the increment in the line width is also 100 μm. The lines of "ones" are the scratches of depth h, while the lines of "zeros" correspond to the unperturbed substrate. Reconstructed optical path variation across the substrate for a fixed bandwidth λ_min=150 μm (ν_max=2 THz) and variable scratch depths (b) h=75 μm, (c) h=100 μm, (d) h=125 μm, (e) h=150 μm and (f) h=250 μm.

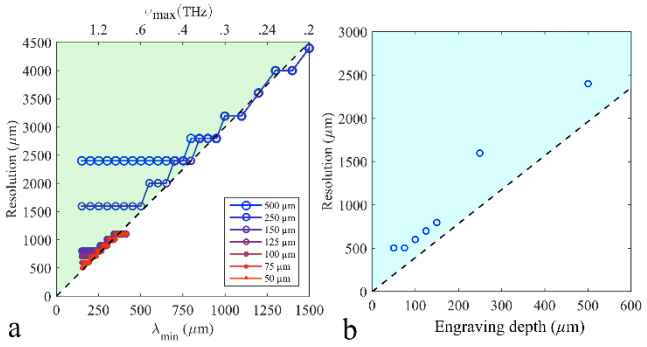


**Fig. S7. Image resolution, case of the phase masks.** (a) Resolution as a function of the THz bandwidth for different values of the engraving depth $h$ (shown in the legend). The green region corresponds to the resolvable region set by the Nyquist theorem $\delta x > 0.5\lambda_{\min}F/\rho_0$, (b) Resolution as a function of the engraving depth $h$ for a fixed THz bandwidth ($\lambda_{min}$=150 μm, $\nu_{max}$=2 THz). The blue region corresponds to the resolvable region as defined by the equation $\delta x > h(n_m - n_a)\,F/\rho_0$.

## REFERENCE

1. F. Ellrich, T. Weinland, D. Molter, J. Jonuscheit, and R. Beigang, "Compact fiber-coupled terahertz spectroscopy system pumped at 800 nm wavelength," Rev. Sci. Instrum. **82**(5), (2011).